Influence of rain on air-sea gas exchange: Lessons from a model ocean

David T. Ho,[1,2] Christopher J. Zappa,[3,4] Wade R. McGillis,[3,4] Larry F. Bliven,[5] Brian Ward,[3] John W. H. Dacey,[6] Peter Schlosser,[1,2,7] and Melissa B. Hendricks[8]

[1] Rain has been shown to significantly enhance the rate of air-water gas exchange in fresh water environments, and the mechanism behind this enhancement has been studied in laboratory experiments. In the ocean, the effects of rain are complicated by the potential influence of density stratification at the water surface. Since it is difficult to perform controlled rain-induced gas exchange experiments in the open ocean, an SF_6 evasion experiment was conducted in the artificial ocean at Biosphere 2. The measurements show a rapid depletion of SF_6 in the surface layer due to rain enhancement of air-sea gas exchange, and the gas transfer velocity was similar to that predicted from the relationship established from freshwater laboratory experiments. However, because vertical mixing is reduced by stratification, the overall gas flux is lower than that found during freshwater experiments. Physical measurements of various properties of the ocean during the rain events further elucidate the mechanisms behind the observed response. The findings suggest that short, intense rain events accelerate gas exchange in oceanic environments. INDEX TERMS: 0312 Atmospheric Composition and Structure: Air/sea constituent fluxes (3339, 4504); 4504 Oceanography: Physical: Air/sea interactions (0312); 4572 Oceanography: Physical: Upper ocean processes; KEYWORDS: gas exchange, rain, SF6, turbulence, stratification

1. Introduction

[2] On global and regional scales, air-water gas exchange is an important process that strongly influences the budgets of biogeochemical trace gases, as well as the transport of volatile pollutants between the atmosphere and a water body. For these reasons, it is crucial to understand the mechanisms that control the rate of air-water gas exchange.

[3] Near-surface turbulence is presumed to be the dominant mechanism regulating the transfer velocity, k, of slightly soluble gases across the air-water interface in the absence of bubbles. The magnitude of k is determined by diffusion through a spatially and temporally varying boundary layer, the thickness of which is a function of near-surface turbulence and diffusion.

[4] Considerable effort has been spent on determining empirical relationships between k and wind speed [e.g., *Liss and Merlivat*, 1986; *Nightingale et al.*, 2000; *Wanninkhof*, 1992; *Wanninkhof and McGillis*, 1999], since wind speed is relatively easy to measure and plays a central role in the generation of turbulence through the transfer of momentum to waves and currents at the ocean surface. For a wind-driven system, turbulence is generated near the air-water interface through shear, buoyancy, or large- and micro-scale wave breaking, among other processes. There is increasing evidence that k may strongly correlate with air-water surface roughness or the mean square slope of short wind waves [e.g., *Bock et al.*, 1999; *Jähne et al.*, 1987]. In the presence of surface films, k may be significantly reduced at a given wind speed or wind stress [*Asher and Pankow*, 1986; *Jähne et al.*, 1987, 1979, 1985]. Surfactants can significantly dampen waves at high wave numbers and thus affect wave slope spectra [*Frew*, 1997]. This change in the wave spectra is linked to reduced gas exchange [*Bock et al.*, 1999]. Microscale wave breaking has been suggested as a dominant mechanism for gas exchange at low to moderate wind speeds over the ocean [*Zappa et al.*, 2001] (see also C. J. Zappa et al., Microbreaking and the enhancement of air-water gas transfer velocities, submitted to *Journal of Geophysical Research*, 2004) (hereinafter referred to as Zappa et al., submitted manuscript, 2004) and may explain the observed correlation between k and surface roughness. Regardless of the specific processes and details of the underlying physics, models

---

[1]Lamont-Doherty Earth Observatory, Columbia University, Palisades, New York, USA.

[2]Also at Department of Earth and Environmental Sciences, Columbia University, New York, New York, USA.

[3]Applied Ocean Physics and Engineering Department, Woods Hole Oceanographic Institution, Woods Hole, Maryland, USA.

[4]Now at Lamont-Doherty Earth Observatory, Columbia University, Palisades, New York, USA.

[5]NASA/GSFC, Laboratory for Hydrospheric Processes, Wallops Island, Virginia, USA.

[6]Biology Department, Woods Hole Oceanographic Institution, Woods Hole, Massachusetts, USA.

[7]Also at Department of Earth and Environmental Engineering, Columbia University, New York, New York, USA.

[8]Department of Geosciences, Princeton University, Princeton, New Jersey, USA.

generally attempt to parameterize k based on the assumption that turbulence regulates the exchange.

[5] Laboratory experiments and preliminary field studies show that raindrops falling on a freshwater surface significantly enhance k. Rain-induced gas exchange systematically increases with the kinetic energy flux (KEF) to the water surface supplied by the raindrops [*Ho et al.*, 2000, 1997]. The enhancement in k by rain is dominated by the production of turbulence and secondary motions, whereas rain-generated bubbles contribute 0–20% of the total gas exchange, depending on rain rate, raindrop size, and gas solubility [*Ho et al.*, 2000]. These findings suggest a possible mechanism for increasing the rate of air-water gas exchange in quiescent environments with little wind-forcing.

[6] Until now, all experiments aimed at quantifying rain-induced gas exchange have been performed in freshwater. The main difference between rain falling on freshwater and salt water is the resulting stratification of the upper water column in the case of a saltwater body. Rain promotes density stratification that inhibits turbulent mixing, but might also generate density-driven circulation, which can contribute to water column turbulence. Near-surface shear associated with rain-induced density stratification may affect the turbulence in the surface aqueous boundary layer and the ability to predict k. Thus the behavior and properties of these processes need to be understood and measured for development of adequate models for rain-induced gas exchange.

[7] Because it is difficult to conduct controlled experiments in the open ocean, the Biosphere 2 ocean was chosen for pilot studies of rain-induced air-sea gas exchange. The facility is ideally suited for such an experiment because (1) the processes that are responsible for rain-induced gas exchange in the Biosphere 2 ocean should be similar to those in the real ocean; (2) most of the ceiling height above the Biosphere 2 ocean is greater than 13 m, which allows realistic rain to be generated (i.e., raindrops of reasonable size approaching terminal velocity); and (3) the presence of a wave generator offers the possibility of studying gas exchange driven by both the interaction of a wavy surface and the additional effect of rain.

[8] In the following, we present the results of an experiment conducted at the Biosphere 2 Center: Bio2 RainX II. The gas transfer velocity was determined by performing an SF_6 evasion experiment. Raindrop size distributions were measured with a Rain Imaging System (RIS), records of high-resolution temperature and salinity gradients were made using the Skin Depth Experimental Profiler (Skin-DeEP), surface wave fields were measured using a laser altimeter, 3-D current fields were measured using a bottom mounted acoustic Doppler current profiler (ADCP), turbulence measurements were performed with three acoustic Doppler velocimeters (ADV), and the thermal signature of water surface was measured using an infrared (IR) imager. Together, these measurements allow us to study the influence of rain on air-sea gas exchange, as well as to elucidate the mechanisms responsible for the observed effect.

2. Methods

[9] During Bio2 RainX II, three rain experiments were conducted. The first (RE1) was a short rain event (53 min), during which equipment was tested. The second (RE2) was a

longer rain event (122 min), during which an SF_6 evasion experiment was conducted. The third (RE3) was a very short event (15 min) during the night, when infrared measurements were made. The length of RE2 was dictated by the fresh water storage capacity of the reservoirs and by the range of tolerable water level in the ocean, as well as the salinity limit imposed by the requirements of organisms in the ocean.

2.1. Biosphere 2 Ocean

[10] The Biosphere 2 ocean contains 2650 m^3 of saltwater with a nominal salinity of 35.5. It has a surface area of approximately 675 m^2 and an average depth of 3.5 m. The ocean is maintained at a constant temperature of 26.5°C by pumps that circulate the ocean water through a heat exchanger. On one side of the ocean, there is a vacuum wave generator capable of creating sufficiently energetic waves to circulate water in the ocean and enough turbulence to enhance air-water gas exchange. The entire length of the wave wall is partitioned into five sections of enclosed air space above the water surface. A vacuum is applied to the chambers, and the water level inside rises. When the water reaches a specified height, the vacuum is relaxed to atmospheric pressure and the water level falls, causing water to rush out of the chambers, and creates waves that propagate toward the beach (Figure 1). Wave amplitude is regulated by the water level in the chambers, which in turn is controlled by the pumping rate of the vacuum, and the frequency of the wave is regulated by the timing of the valves that apply and relieve the vacuum. For a more detailed description of the Biosphere 2 ocean, see *Atkinson et al.* [1999].

2.2. Rain Generator

[11] Two water reservoirs (36 and 57 m^3) were used to supply water to the rain generation system, via 10 cm OD PVC pipes and two 15 horsepower multistage centrifugal pumps. The tanks contained groundwater that had been purified by reverse osmosis to remove nutrients and other contaminants.

[12] The system used for generating rain during Bio2 RainX II consisted of a series of eight 2.5-cm OD polyvinylchloride (PVC) pipes hanging off messenger wires strung across the ocean. Attached to each pipe were three rain heads, for a total of 24 rain heads. The rain heads were modified commercially available irrigation devices (Rain Bird Xeri-Bird 8 MultiOutlet Emission Device) with short pieces of 0.3-cm ID latex tubing secured to the eight emitter nozzles on each device. The heads were oriented with the tubing facing up (head inverted) with pipe stems descending from the overhead 2.5-cm OD PVC pipes. The flow regulators were removed from each device, allowing for a higher flow rate of 15 L min^{-1}. The flexible tubing encouraged random dispersion of the drops, as well as a spectrum of drop sizes to be generated. The rain heads were located 13 m above the ocean, allowing raindrops to achieve terminal velocity before impacting the surface.

2.3. SF_6 Evasion Experiments

[13] To assess the effect of rain on air-sea gas exchange, an SF_6 tracer release experiment was conducted during RE2. A predetermined amount of SF_6 dissolved in water ($\sim 1.3 \times 10^{-5}$ moles) was injected into the ocean using a 60-mL syringe 12 hours in advance of RE2. Thorium
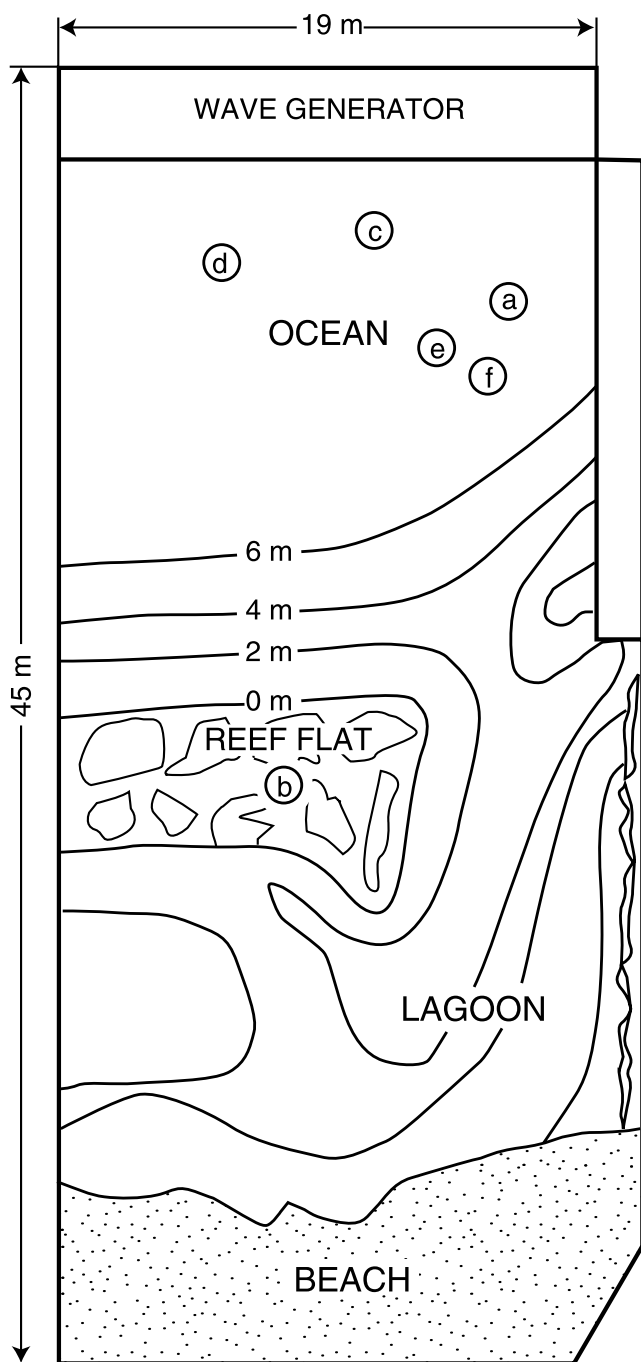
Figure 1. The Biosphere 2 ocean, 45 m long, 19 m wide, with depth of the bottom varying from about 0.5 to 7 m. Indicated are the location of various instruments during Bio2 RainX II: a, SF_6 and salinity sampler, and laser slope zero-crossing meter; b, Rain Imaging System (RIS); c, Skin Depth Experimental Profiler (SkinDeEP); d, laser wave height altimeter, and acoustic Doppler current profiler (ADCP); e, acoustic Doppler velocimeters (ADV) mounted on SPIP; f, area measured by an infrared imager.

isotope [*Atkinson et al.*, 1999] and SF_6 measurements (Bio2 RainX I, unpublished data, 2001) have shown that the Biosphere 2 ocean mixing time is of the order of a few hours. SF_6 measurements made during a pilot rain experiment showed that the tracer remained laterally well mixed in

the Biosphere 2 ocean during the rain events (Bio2 RainX I, unpublished data, 2001). The transfer velocity for no rain conditions ($R = 0$) was determined by measuring the decrease in SF_6 concentration as a function of time in the ocean in the absence of rain over a period of 20 hours. Immediately prior to RE2, samples for SF_6 were taken to establish the initial concentration. The gas transfer velocity during RE2 was determined by measuring the decrease of SF_6 in the water with corrections applied for dilution due to addition of SF_6-free rainwater (see below).

2.4. Water Sample Collection and Measurement

[14] A specially designed sample profiler allowed water to be drawn from different depths in the ocean for salinity and SF_6 measurements. The profiler consisted of a $5 \times 60 \times 60$ cm polystyrene float, and 14 lengths of 0.3175 cm ID flexible vinyl tubing, secured at different depths relative to the float along a weighted line. The float kept the sampling ports at fixed depths relative to the water surface (2, 3, 4, 6, 9, 17, 30, 49, 69, 90, 134, 210, 393, 596 cm) as the water level rose during rain and as waves passed the sampling point. The profiler was secured in place at a fixed location in the ocean by attachment to a boom extending away from the edge of the ocean.

[15] The inlet of each tube was protected with a screen to prevent blockage of tubing by sediments and organic matter in the ocean. During a typical sampling procedure, the tubing was attached to a peristaltic pump, and water was drawn at a rate of ~100 mL min^{-1}, which filled a measurement cell attached to a conductivity probe on a YSI 6600 multiparameter sonde. Each salinity measurement was completed when its value reached steady state, and the measurement cell was allowed to drain before refilling with sample from the next depth. During and after the rain event, the depths were sampled out of sequence to ensure that measurements at a given depth did not affect adjacent depths. Any bubbles forming on the conductivity cell were removed by lightly agitating the sonde.

[16] After completion of the salinity measurement, a three-way valve at the top of the sampling line was closed to prevent drainage back down the tube, and the peristaltic pump was disconnected. A 50-mL glass syringe was connected to the three-way valve, the valve was opened and water was drawn slowly into a 50-mL glass syringe for SF_6 measurement. During water sampling for SF_6, extreme care was taken to prevent the occurrence of bubbles in the sampling line or in the syringe. No samples were kept for analysis when bubbles were seen in the tubing or in the syringe.

[17] SF_6 analyses were conducted using a headspace method described by *Wanninkhof et al.* [1987]. Glass syringes were filled to 30 mL of water, and then a headspace of 20 mL was created with ultra-high purity (UHP; 99.999%) N_2. The syringes were then shaken vigorously on a mechanical shaker for 3 min to equilibrate the water with the N_2 in the headspace. The gas sample in the headspace was then pushed through a drying column of $Mg(ClO_4)_2$ and into a sample loop. Subsequently, the sample was injected into a gas chromatograph equipped with an electron capture detector (GC-ECD) using UHP N_2 as carrier gas. SF_6 was separated from other gases at room temperature with a Molecular Sieve 5A column.

[18] During the RE2, samples were collected every 20 min at a fixed site from 14 depths in the ocean. Sampling for SF_6 and salinity continued for 24 hours after the rain stopped to examine how the ocean relaxes to an equilibrium state, and to estimate k in the absence of rain.

2.5. Tracer Dilution Models and Gas Exchange Calculations

[19] The observed decrease in total tracer concentration in the ocean during the experiments was caused by gas exchange at the air-water interface and by dilution of ocean water by SF_6-free rain. In order to separate the gas exchange component from the dilution component, the following dilution correction has to be applied to the measured SF_6 concentration $C_m(z)$ in order to obtain a corrected SF_6 concentration $C(z)$,

$$C(z) = C_m(z) \frac{s(z)}{s_0}, \tag{1}$$

where s_0 is the initial salinity of the ocean before the rain and $s(z)$ is the salinity measured concurrently with $C_m(z)$.

[20] For each profile, the mean SF_6 concentration in the ocean is determined by

$$C = \frac{1}{V_{tot}} \int_{z_{tot}} C(z)V(z)dz, \tag{2}$$

where $C(z)$ is the concentration of SF_6 measured at a certain depth z, $V(z)$ is the volume of the ocean in the depth range represented by z (Figure 2), and V_{tot} and z_{tot} are the total volume and depth of the Biosphere 2 ocean, respectively. The gas flux across the air-water interface, F, is related to the total change in mean SF_6 concentration in the ocean with time by

$$F = h \frac{dC}{dt}, \tag{3}$$

where h is the mean depth of the ocean. The gas transfer velocity, k, is described by

$$k = \frac{F}{(C_w - \alpha C_a)}, \tag{4}$$

where C_w is the SF_6 concentration in the water directly below the air-water interface, and αC_a is the solubility equilibrium for SF_6 in the water. If the water is well mixed with respect to tracer concentration, equations (3) and (4) are combined, assuming that $C_w = C$, and integrating over Δt to obtain

$$k = \frac{h}{\Delta t} \ln \frac{(C_i - \alpha C_a)}{(C_f - \alpha C_a)}, \tag{5}$$

where C_i and C_f are the initial and final mean tracer concentrations in the ocean, respectively. If there is a significant vertical gradient in tracer concentration, then equations (3) and (4) are combined to yield [Ledwell, 1982]

$$k = h \frac{dC/dt}{(C_w - \alpha C_a)}. \tag{6}$$

Equation (6) was used to calculate a gas transfer velocity from the tracer data. SF_6 in the Biosphere 2 atmosphere, C_a,
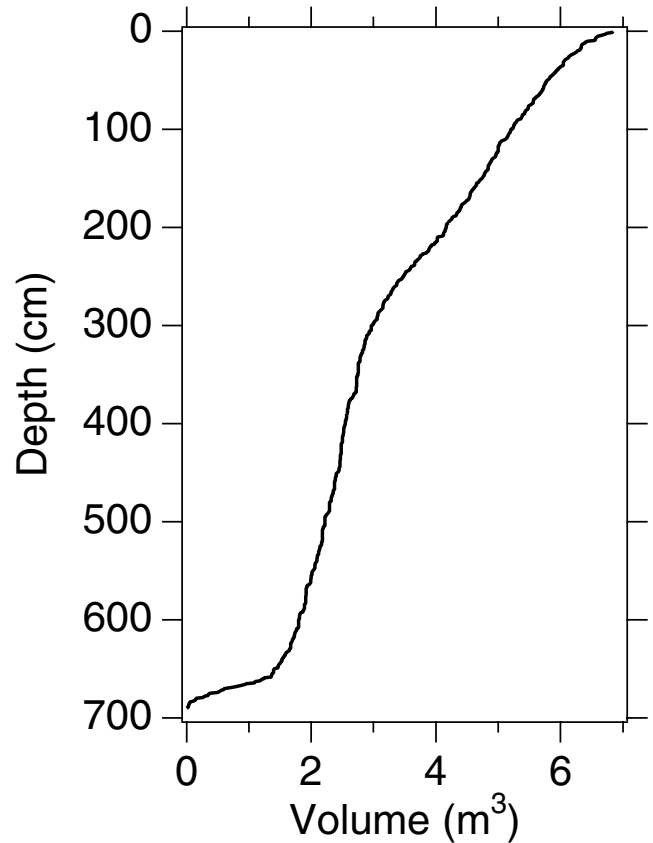
Figure 2. Volume of the Biosphere 2 ocean as a function of depth.

was non-negligible and was determined by sampling with 50-mL glass syringes and measurement using the GC-ECD.

[21] The gas transfer velocity for SF_6 was normalized to a Schmidt number (Sc) of 600, corresponding to values for CO_2 at 20°C using the relationship

$$k(600) = k_{SF_6} \left(\frac{600}{Sc_{SF_6}} \right)^n, \tag{7}$$

where k_{SF_6} and Sc_{SF_6} are the gas transfer velocity and the Schmidt number for SF_6 (782 for our experiment), respectively. Sc is defined as the ratio of the kinematic viscosity of water, v, to the diffusion coefficient of gas in water, D_g. It has been shown in models and experiments that for a clean wavy water surface, in the absence of bubbles, n equals $-1/2$ [Brumley and Jirka, 1988; Jähne et al., 1984; Ledwell, 1984].

2.6. Rain Rate and Drop Size Distribution

[22] During Bio2 RainX II, the raindrop size distribution (DSD) was obtained from data provided by a Rain Imaging System (RIS) developed at NASA. RIS is an optical system consisting of an analog black and white video camera that is pointed at a halogen flood lamp. The 100–300 mm lens was adjusted so that the center of the focal volume is located at 2 m from the camera. The field of view is 32 × 24 mm, and the depth of field is 13.6 mm. The distance between the camera and the light source was 3 m, so there was no significant droplet splash from the instrument into the

measurement volume. The RIS camera and light were located on the coral reef as shown in Figure 1, and RIS was connected to an image analysis personal computer located on the beach area. The video data were compressed and archived for later processing.

[23] Digital images were obtained at a rate of approximately 50 Hz. Each image consists of 640 × 240 pixels. The pixel size is 0.05 × 0.1 mm and is adequate to identify and characterize drops larger than 0.5 mm diameter. The halogen lamp provides sufficiently bright illumination so that the camera operates with the shutter speed of 1/100,000 s. The terminal velocity of the water drops increases with drop size, such that for 1- to 5-mm drops, it varies from 2 to 5 m s^{-1}. Together, the shutter speed, frame rate, and image cross section yield independent images that have insignificant blurring due to motion [see *Saylor et al.*, 2002]. Each water drop presents a distinctive pattern: A water drop within the focal volume appears as a disc with a hole; a drop just outside of the focal volume appears as a solid disc; and drops still farther away from the focal volume lack sufficient contrast to be analyzed.

[24] The images were processed using a four-step algorithm: (1) a pixel scaling procedure to account for nonuniform illumination, (2) a threshold process to distinguish dark areas from bright ones, (3) a pattern recognition process to select only drops within the measurement volume, and (4) a particle sizing measurement to obtain the equivalent drop diameter. Equivalent drop diameter is a sizing measure that relates the observed area to that of a circle. Video data were obtained with the RIS during the entire experiment and all the images were analyzed to compute the DSD. Computations by *Craeye and Schlussel* [1998] of drop velocity versus dropping height for various drop sizes show that for a fall height of 10 m, drops as large as 5 mm are within a few percent of terminal velocity. At the Biosphere 2 facility, the 13-m fall height of the drops is sufficient for drops to approach terminal velocity. Thus a relationship developed by *Lhermitte* [1988] was used as a realistic estimate of drop velocities v in the RIS measurement volume,

$$v(D) = 9.25 - 9.25 \exp\left[-\left(6.8D^2 + 4.88D\right)\right], \qquad (8)$$

where D is drop diameter in mm and v has units of m s^{-1}. *Ho et al.* [1997] proposed that rain-induced air-water gas exchange is correlated to rain kinetic energy flux (KEF). KEF can be derived from a DSD according to

$$\mathrm{KEF} = \frac{\rho}{2} 0.6\pi \int v(D)^2 N(D) D^3 dD, \qquad (9)$$

where ρ is the density of water and KEF has units J m^{-2} s^{-1}.

[25] During Bio2 RainX II, the spatial distribution of the simulated rain was assessed using water volume measurements from twelve 10-cm-diameter buckets. The buckets sat on floats, which were each tethered by a 1-m line to one of two ropes that extended from the wave generator to the beach.

2.7. High-Resolution Temperature and Salinity Profiles

[26] SkinDeEP, an instrument designed to make high-resolution profiles within the upper 10 m of the ocean, was deployed during Bio2 RainX II to study the evolution of the cool freshwater lens both during and after the rain events. SkinDeEP operates autonomously by changing its density. Positive buoyancy is achieved by pumping air from inside the body of the profiler into an external neoprene inflatable sleeve. The instrument sinks when the sleeve is deflated by returning the air to the interior. The instrument is equipped with millimeter resolution temperature and conductivity sensors mounted some distance from the top end-cap. Data are recorded only during the ascending phase of the profile when sensors are out of the wake of the instrument. For a more thorough description of the instrument, see *Ward et al.* [2004].

[27] During the experiment, SkinDeEP was deployed at the deep end of the ocean (6.5 m), adjacent to the wave generator (Figure 1). Profiles were measured over the upper 4 m, as the height of SkinDeEP with sensors attached is 2 m. The instrument was tethered to the ocean floor in order to maintain its location. SkinDeEP came to the end of its tether only after its sensors had penetrated the air-water interface.

[28] Table 1 provides a summary of the deployment times, profile interval, and number of profiles for RE1 and RE2. For the RE1, SkinDeEP made profiles for 6 hours at an interval of about 2 min. The instrument was in a lower power mode between profiles. The total number of profiles collected during this period was 164. For RE2, SkinDeEP was deployed well in advance of the rain. The initial profile rate was approximately 2.5 min, until the rain event ceased, whereupon SkinDeEP was recovered and the on-board computer reprogrammed to reduce the profile rate to about 7 min. This operation was carried out to extend the measurement period of SkinDeEP.

2.8. Turbulence Measurements

[29] The Surface Processes Instrument Platform (SPIP) is a 2-m research catamaran used to measure the turbulence near the air-water interface. The location of SPIP during Bio2 RainX II is shown in Figure 1. It was moored in the ocean such that the bow was directed into the dominant current flow, allowing for turbulence measurements right at the surface with potentially less flow distortion than other surface-mounted instrumentation. The bow of SPIP was outfitted with three SonTek 3-axis acoustic Doppler velocimeters (ADVs) at nominal depths of 5 cm, 25 cm, and 60 cm. The ADVs provided a point measurement of x-, y-, and z-axis velocity components (u, v, and w, respectively). Mean flow velocity and turbulent velocity (dissipation rate) statistics were estimated from 15-min records sampled at 25 Hz.

Table 1. Summary of SkinDeEP Operations During Bio2 RainX II

Rain Event	SkinDeEP Start, Local Time	SkinDeEP Stop, Local Time	Mean Profile Interval, min	Number of Profiles
RE1	Mar13 1054	Mar13 1656	2.2	164
RE2[a]	Mar18 0924	Mar18 1347	2.6	100
RE2[b]	Mar18 1440	Mar19 1313	6.9	191

[a]During rain (high resolution).
[b]After rain (low resolution).

[30] In steady flow with isotropic, fully-developed turbulence, kinetic energy cascades from large eddies to smaller eddies which finally dissipates through viscosity. Under these conditions, the turbulent dissipation rate, ε, can be estimated by the magnitude of the wave number spectrum in the inertial subrange. The inertial dissipation method is used to determine ε,

$$S = K\varepsilon^{2/3}\kappa^{-5/3}, \tag{10}$$

where S is the wave number spectrum of the fluctuating vertical velocity, w, $\kappa = 2\pi f/V$ is the wave number, V is the mean surface current, f is the frequency, and K is Kolmogorov's empirical constant of 0.52.

[31] Measurements of ε were made in the Biosphere 2 ocean according to this model for the inertial subrange of the kinetic energy spectrum in equation (10) using an ADV. The ADV sampled the three components of water velocity at 25 Hz, and frequency spectra were measured using the sensor at the 25-cm depth. The frequency spectra were measured and corrected for pulse averaging by dividing the measured frequency spectra by the factor $[\sin(\pi f\Delta t)/\pi f\Delta t]^2$. Assuming Taylor's hypothesis of frozen turbulence, the frequency spectra were then converted to wave number space by $\kappa = 2\pi f/V$, and ε is calculated directly from equation (10). A safe lower bound of the inertial range for these data was determined to be 20 rad m^{-1} according to the criterion $\kappa z > 5$. A reasonable upper bound was determined to be 80 rad m^{-1} according to the criterion $\kappa L < 1$, where L is the length scale of the sample volume ($L = 1$ cm for the ADV used in this study).

[32] In an effort to relate the concept of surface renewal [*Danckwerts*, 1951] directly to near-surface turbulence, *Lamont and Scott* [1970] developed a hydrodynamic model based upon viscous eddies characteristic of the shortest timescale. The continual replacement of water in the aqueous molecular boundary layer (MBL) through surface renewal has been suggested as a fundamental hydrodynamic process controlling gas exchange and has resulted in a useful conceptual model for k. Surface renewal models describe the continuous random renewal of the aqueous MBL with the bulk water below due to turbulent eddies. The idealized process is one in which renewal is complete and instantaneous. As turbulent eddies renew the surface, bulk water parcels that are not in equilibrium with the atmosphere come in contact with the interface and exchange gas with the atmosphere through diffusion. The faster this renewal occurs, the higher the k. Therefore, surface renewal models predict k as

$$k \propto \left(D_g/\tau\right)^{1/2} = \left(D_g\lambda\right)^{1/2}, \tag{11}$$

where τ is the lifetime of a parcel of water exposed to diffusion at the surface, or alternatively $\lambda = 1/\tau$ is the surface-renewal rate. Estimating τ by the Kolmogorov, or dissipative timescale, $(\nu/\varepsilon)^{1/2}$, the near-surface hydrodynamics are directly proportional to $\varepsilon^{1/4}$, and k is expressed as

$$k \propto (\varepsilon\nu)^{1/4}Sc^{-n}. \tag{12}$$

This scaling demonstrates that increasing turbulence intensity will enhance k, and this scaling has been tested with success in the laboratory for varying surface conditions [*Asher and Pankow*, 1986].

2.9. Wave and Current Measurements

[33] A laser altimeter (Riegl LD90-3100 VHS) was mounted from the space frame directly above the acoustic Doppler current profiler (described below) in the Biosphere 2 ocean in order to characterize the wave field that existed during Bio2 RainX II. It measured the surface elevation to within ±0.3 cm at a sample frequency of 20 Hz. Measurements were made continuously for RE2 as well as RE3 and wave statistics were determined from 15-min records. Significant wave height was calculated from the RMS of the surface elevation, and the dominant wave frequency was determined as the peak in the power spectra of surface elevation.

[34] The laser slope zero-crossing meter, a prototype system that characterizes the surface wave slope, was deployed in the Biosphere 2 ocean. It uses a 3mW diode laser at 680 nm as a submerged light source and a silicon photodiode detector on the airside. The photodiode detector samples at 200 Hz and senses the maximum intensity when the surface is flat. Therefore the inverted squared laser light intensity, σ, is defined such that higher values denote a water surface that is abundant with small-scale, steeply sloped waves.

[35] A 1200-kHz acoustic Doppler current profiler (ADCP) was deployed at the bottom of the ocean on the east side near the 6-m depth. The ADCP profiled the water column at 1-s intervals with 20-cm bins to measure the predominant currents and shear. Velocities were measured in 5-min averages. The ADCP was deployed continuously during the experiments.

2.10. Passive Thermal Infrared Imagery Measurements

[36] Just as the gases move through the surface boundary layer by diffusion, heat fluxes through the aqueous thermal boundary layer (TBL) by molecular conduction at the surface [*Katsaros*, 1980; *Robinson et al.*, 1984]. Because of evaporation, the temperature at the water surface, or skin, is typically less than the bulk temperature immediately below by several tenths of a degree Celsius [*Donlon and Robinson*, 1997; *Schlüssel et al.*, 1990; *Wick et al.*, 1996]. This thin, gravitationally unstable TBL is of $O(10^{-3}$ m) thick or less [*Hill*, 1972; *McAlister and McLeish*, 1969; *Wu*, 1971], and exists for a variety of forcing, including shear-driven [*Saunders*, 1967] and buoyancy-driven [*Katsaros*, 1977; *Katsaros et al.*, 1977] turbulent processes. Depending on the relative amount of shear and buoyancy, vertical and horizontal structure can be complex due to the variability of the near-surface turbulence mechanisms and due to the supporting heat flux [*Zappa et al.*, 1998].

[37] Passive infrared (IR) imagery measures the detailed micro-scale horizontal structure in skin temperature and can be used as a visualization tool for turbulence at water surfaces. An IR imager is ideally suited to measure the skin temperature because the optical depth of the infrared radiation detected, roughly $O(10^{-5}$ m) [*McAlister*, 1964; *McAlister and McLeish*, 1970], is much less than the thickness of the TBL. Recently developed IR imaging techniques have quantified signatures of thermal variability

that result from renewal processes such as large-scale wave breaking [*Jessup et al.*, 1997], microbreaking [*Zappa*, 1999; *Zappa et al.*, 2001, submitted manuscript, 2004], near-surface shear, and free-convective patchiness [*Zappa et al.*, 1998]. Similarly, rain will generate turbulence directly at the air-water interface and will contribute to, if not dominate, the disruption of the TBL. Therefore, IR measurements of the temporal and spatial characteristics of skin temperature variability provide the capability to remotely monitor free-surface turbulence.

[38] An IR imaging system (Amber LWIR camera) was implemented for visualizing the turbulence caused by the rain. It was mounted 9.5 m above the ocean almost normal to the surface for thermal imaging the aqueous thermal boundary layer. This configuration resulted in roughly a 2 × 2 m image size with less than 1-cm resolution, and the IR imagery was digitized at a frequency of 30 Hz. The noise equivalent temperature difference (or mean resolvable temperature difference) was determined to be ±0.02°C using a blackbody isothermal calibration target; k was determined from equation (11) by estimating the λ from IR imagery. During a renewal event, the surface temperature will increase abruptly and diffusion will subsequently cause the surface temperature to decrease. Here λ was estimated from a peak in the frequency spectrum of the surface temperature measured by the IR imagery both before and during the rain events; λ was also determined by counting the sharp abrupt temperature increases, or spikes in temperature, divided by the total measurement time. The estimate for the heat transfer velocity, k_H, from equation (11) was related to $k(600)$ using equation (7), where k_{SF_6} and Sc_{SF_6} are replaced by k_H and the Prandtl number, Pr, respectively.

3. Results

3.1. Rain Rate and Drop Size Distribution

[39] During Bio2 RainX II, RIS recorded 53 and 122 min of rain for RE1 and RE2, respectively, and the DSDs for both rain events are similar. The DSD for RE2 is shown in Figure 3, and is derived from more than 52,000 drops. The DSD reveals a shape that is commonly observed in natural rain, i.e., decreasing drop density as the drop size increases. RIS measured drops from 0.3 to 5.9 mm diameter, so that is the dropsize range that was used to compute rain rates and KEFs. To compare the simulated rain to natural conditions, DSD for Marshall-Palmer (M-P) distribution [*Marshall and Palmer*, 1948] is also shown in Figure 3. The M-P distribution is given by

$$N(D) = N_0(R) \exp(-\Lambda D), \tag{13}$$

where $N_0 = 8 \times 10^4$ m^{-3} cm^{-1} and $\Lambda = 42.3 \times R^{-0.214}$ cm^{-1} from *Olsen et al.* [1978] are used because R between model input and output is conserved. Figure 3 shows that the DSD measured during RE2 closely resembles the M-P DSD. However, there are some small differences in that the simulated rain tends to be enhanced for drops less than 1.3 mm and tends to be deficient in drops larger than 4.2 mm. Analysis of the two DSDs indicates that during an intense rainfall (~61 mm h^{-1}), assuming the M-P DSD instead of the one measured during RE2 would only underestimate the KEF by 2%.
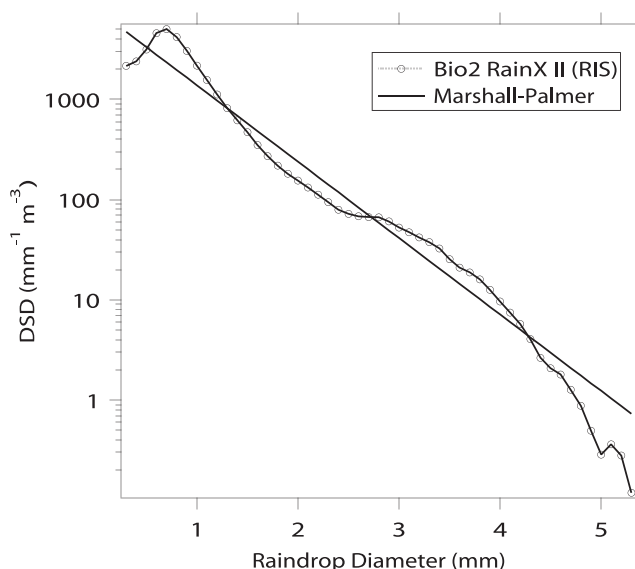
Figure 3. Raindrop size distribution (DSD) measured by RIS during RE2, as well as the Marshall-Palmer DSD. Relative to natural rain, the simulated rain at Biosphere 2 tends to be enhanced for small drops (less than 1.3 mm) and tends to be deficient in larger drops (greater than 4.2 mm). However, kinetic energy fluxes (KEF) computed from the two DSDs are similar because the small drops do not contribute significantly to KEF, and there are few large drops in both DSDs.

[40] Rain rates determined from the bucket data are 76 ± 18 and 68 ± 18 mm h^{-1}, for RE1 and RE2, respectively. Additionally, the standard error between the same buckets for RE1 and RE2 is 24%. These differences are likely due to (1) the circular style spray pattern from the nozzles that are arranged in a rectangular grid; (2) convolution of the 3 × 8 grid pattern of the rain nozzles and a 2 × 6 grid of buckets; and (3) drifting of the buckets on the tether lines.

[41] Hence, although the bucket data provided estimates of the average rain rates, the considerable spatial variability called for a better method to derive average rain rates. The total rise in water level during RE2 was used. The laser altimeter indicated that the water level rose by 10.4 ± 0.3 cm during RE2. Thus the average rain rate for the 122-min experiment was 52 ± 3 mm h^{-1}. This value is in general agreement with the volume of water used and the area of the Biosphere 2 ocean. The DSD measured by RIS is assumed to hold over the entire ocean, so the spatially averaged KEF for RE2 was 0.37 ± 0.02 J m^{-2} s^{-1}.

3.2. Gas Tracer

[42] The observed SF$_6$ concentration in the Biosphere 2 ocean decreases rapidly with the onset of rain. Part of the effect is due to dilution of SF$_6$ tagged ocean water with SF$_6$-free rainwater (about 24% of the total decrease in mean SF$_6$ concentration). However, most of the effect is due to enhanced air-sea gas exchange. The dilution corrected data is shown in Figure 4. With the onset of rain, SF$_6$ is quickly lost from the surface layer (<100 cm).

[43] Figure 5 shows the temporal evolution in mean SF$_6$ concentration in the Biosphere 2 ocean during RE2, and under no rain conditions, respectively. The combined effect
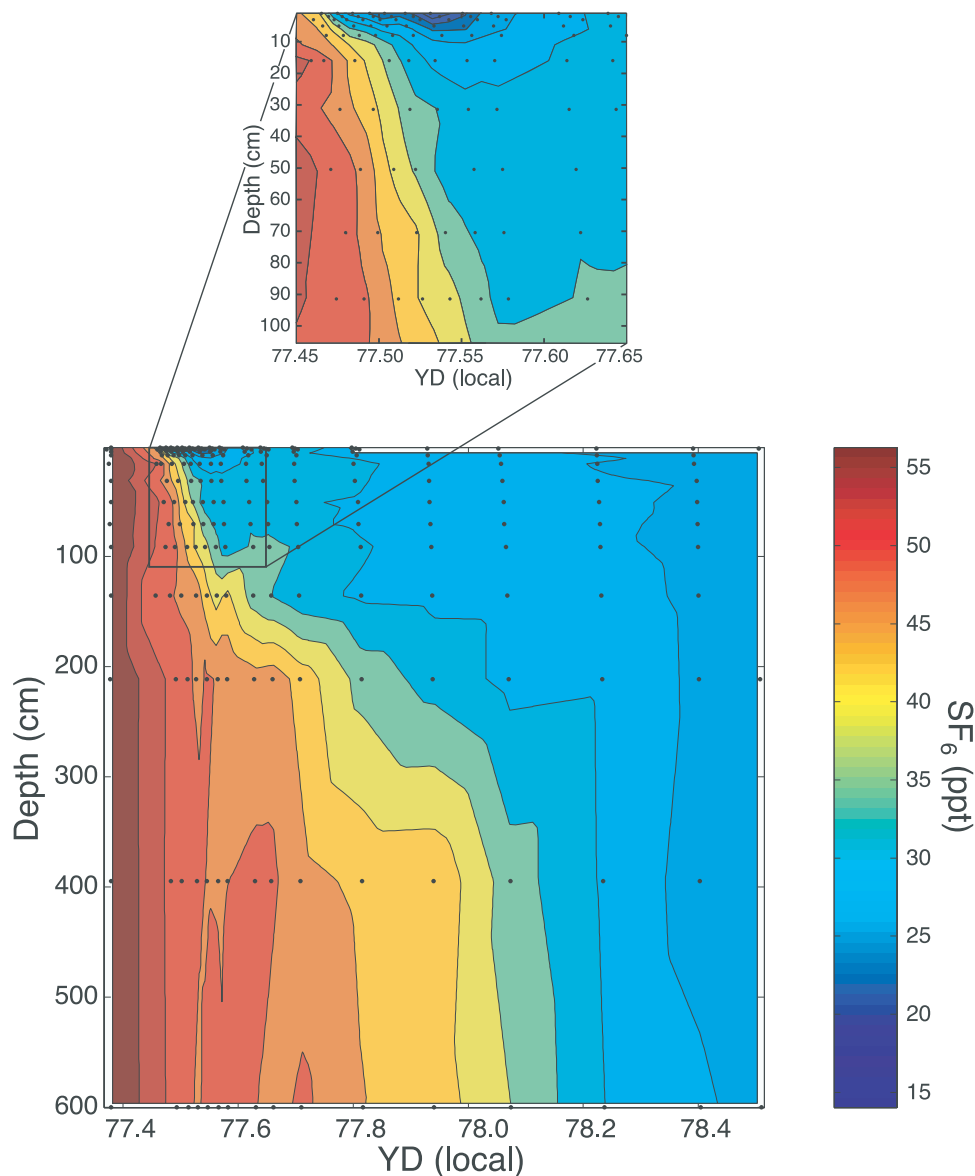
Figure 4. Depth measurements of SF$_6$ concentration as a function of time during RE2. The inset is an enlargement of the top 100 cm of the ocean during the rain event. Each black dot denotes a sample. SF$_6$ concentration has been corrected for dilution according to equation (1).

of the waves generator, circulation pumps, and rain caused the $k(600)$ to be 35.8 ± 4.1 cm h^{-1}. The $k(600)$ for no rain conditions was 8.1 ± 0.2 cm h^{-1}.

### 3.3. High-Resolution Temperature and Salinity Profiles

[44] SkinDeEP was deployed before the start of RE1 and RE2. Salinity profiles for RE1 and RE2 are shown in Figures 6a and 6b, respectively. Salinity is shown instead of density because density changes in the ocean during Bio2 RainX II were dominated by salinity changes. These plots are cross sections through the water column. The two vertical white lines on each figure indicate the start and end times of the rain events.

[45] Before the start of RE1, the salinity was homogeneous throughout the water column (Figure 6a). The presence of the rain had an immediate effect on the surface layer, where a fresh, cool lens developed during the period of the rain. During RE1, the salinity dropped from an initial value of 36 to a minimum of 23.15; the initial temperature was 26.4°C, and reached a minimum of 24.2°C at the surface. After the rain ceased, mixing down of the freshwater resulted in the surface layer gradually reverting to a salinity of 34.4 and a temperature of 26.2°C.

[46] Salinity data from RE2 (Figure 6b) are presented in two sections: one for the high temporal resolution, and the other for the lower resolution. The gap in the data acquisition occurred when the profiler was recovered for reprogramming. The salinity dropped from an initial value of 35.6 to a minimum value of 28.9, which coincided with the end of the rainfall. The water temperature had an initial value of 26.2°C and the cool rain caused this to reduce to 25.0°C. Within 1−2 hours after RE2, the density anomaly was well mixed down to 1 m. Extended sampling following RE2
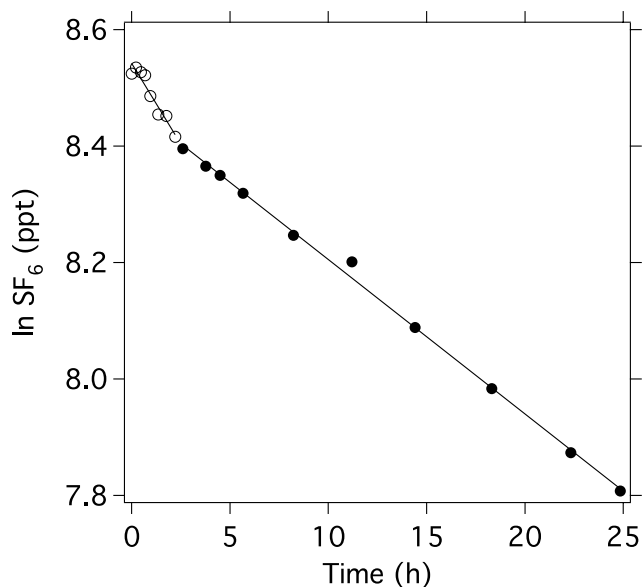
Figure 5. Changes in mean SF_6 concentration in the Biosphere 2 ocean during RE2. Open circles denote rain, and solid circles denote no rain. The SF_6 flux is 110% higher during the rain event.

show that the entire ocean had returned to a homogeneous state around YD 78.

3.4. Near-Surface Turbulence

[47] Measurements of the velocity from the ADVs during all three rain events show similar behavior. Therefore, RE2 is representative of the rain events during Bio2 RainX II. The near-surface RMS horizontal currents are ± 3 cm s^{-1} and vary depending on whether measurements are made before, during, or following the rain events. Prior to the onset of rain, the surface currents were 1 cm s^{-1}, climbing to over 5 cm s^{-1} during the rain event, and falling to 3 cm s^{-1} following the completion of the rain event. These values are consistent with the background column-averaged RMS currents in the ocean of less than 10 cm s^{-1} measured by the ADCP.

[48] Near-surface turbulence is thought to be responsible for air-sea gas transfer, and k has been modeled and shown to scale with ε [Lamont and Scott, 1970]. Figure 7 shows ε at a depth of 20 cm, the shear across a depth of 5 to 20 cm, and the Brunt-Väisälä frequency squared, N^2, across the same depth before, during, and after RE2. The calculation of ε is described above, total shear is calculated according to $\left((du/dz)^2 + (dv/dz)^2\right)^{1/2}$, and N^2 is determined from (g/ρ_o) $(d\rho/dz)$. Prior to the beginning of RE2, ε was 1.0×10^{-5} W kg^{-1}, total mean shear was 0.08 s^{-1}, and N^2 was 1.0×10^{-4} rad^2 s^{-2}. As the rain begins, ε increases abruptly by an order of magnitude to 1.7×10^{-4} W kg^{-1}. Following the peak, ε decreases steadily until the rain terminates and reaches a value of 4.7×10^{-6} W kg^{-1}. Simultaneously with the decrease in ε, total shear steadily increases to a value near 0.2 s^{-1} until the rain ends while N^2 increases to values in excess of 0.03 rad^2 s^{-2}. Following the rain, ε steadily increases to an equilibrium level of 1.1×10^{-5} W kg^{-1}, total mean shear decreases to 0.08 s^{-1}, and N^2 decreases to less than 4.0×10^{-4} rad^2 s^{-2}.

[49] Using ε and equation (12), $k(600)$ was determined to be 10.6 ± 0.6 cm h^{-1} for no rain conditions, and peaked near 21.4 cm h^{-1} during RE2.

3.5. Wave Statistics

[50] During RE2, prior to the onset of rain, the mean wave frequency, f_p, was 0.26 Hz and the mean significant wave height, H_s, was 0.21 m. During the actual rain event, the altimeter was not able to estimate the wave characteristics with statistical reliability since the raindrops act as scatterers for the incident laser pulse. Following the completion of the rain event, f_p had increased to 0.28 Hz and the H_s decreased slightly to 0.20 m. A total of 10.3 cm of rain accumulated in the ocean during RE2. With the rise in Biosphere 2 ocean water level due to the rainfall, the wave generator contributed less wave energy to the ocean by an amount $\rho g h_r$, where h_r is the surface rise due to the rainfall. This likely explains the decrease in significant wave height and corresponding increase in the dominant wave frequency. Note that the total energy lost by the system, $\rho g h_r$, was manifested across the entire spectrum of waves, not only H_s.

[51] While the Riegl laser altimeter had difficulty measuring the wave field during RE2, the laser slope zero-crossing meter deployed near the SF_6 sample profiler during RE1 showed the effect of rain on the small-scale surface slopes generated during the onset of rain (Figure 8). Before the rain begins, relatively constant and low σ is consistent with the observation from the Riegl wave height statistics that the "swell" wave in the Biosphere 2 ocean are long and of low amplitude. As the rain begins, σ abruptly jumps and continues to remain high while decreasing slowly. This suggests that the rain generates significantly small-scale, steeply sloped capillary waves. Following the end of the rain, σ decreases more rapidly as it approaches its pre-rain values, signifying the diminishing of the capillary waves which are no longer generated.

3.6. IR Imagery

[52] In order to obtain data that are not influenced by solar radiation, a night rain experiment (RE3) was performed. Figure 9 shows snapshots of infrared imagery of the Biosphere 2 ocean at successive times over the course of RE3. The temperature variation over the image is approximately 1°C. Warmer regions appear light, and cooler regions are dark. The first image in Figure 9a is a snapshot before a rain event. At this time, the surface is cooler than the water below. The temperature variations reveal small structures created by buoyancy-driven circulation. A look at the movie of infrared imagery also reveals small drift motions caused by the wave field as well as the underlying near-surface current. Figure 9b captures the onset of rain. Airborne rain is observed as black (cool), very fine objects. As rain impacts the water surface, small localized light (warm) patches are generated. The warm patches are caused by energetic mixing disrupting the thin, cool surface layer of $O(1$ mm$)$. Warm water is entrained from below. An individual raindrop causes a disruption of the surface aqueous boundary layer. At this point, the buoyancy-driven background circulation is still apparent. Figure 9c demonstrates that the spatial extent of individual drops eventually will affect the entire ocean surface. Each injected raindrop is seen to influence spatial scales of $O(10$ cm$)$ or less. This
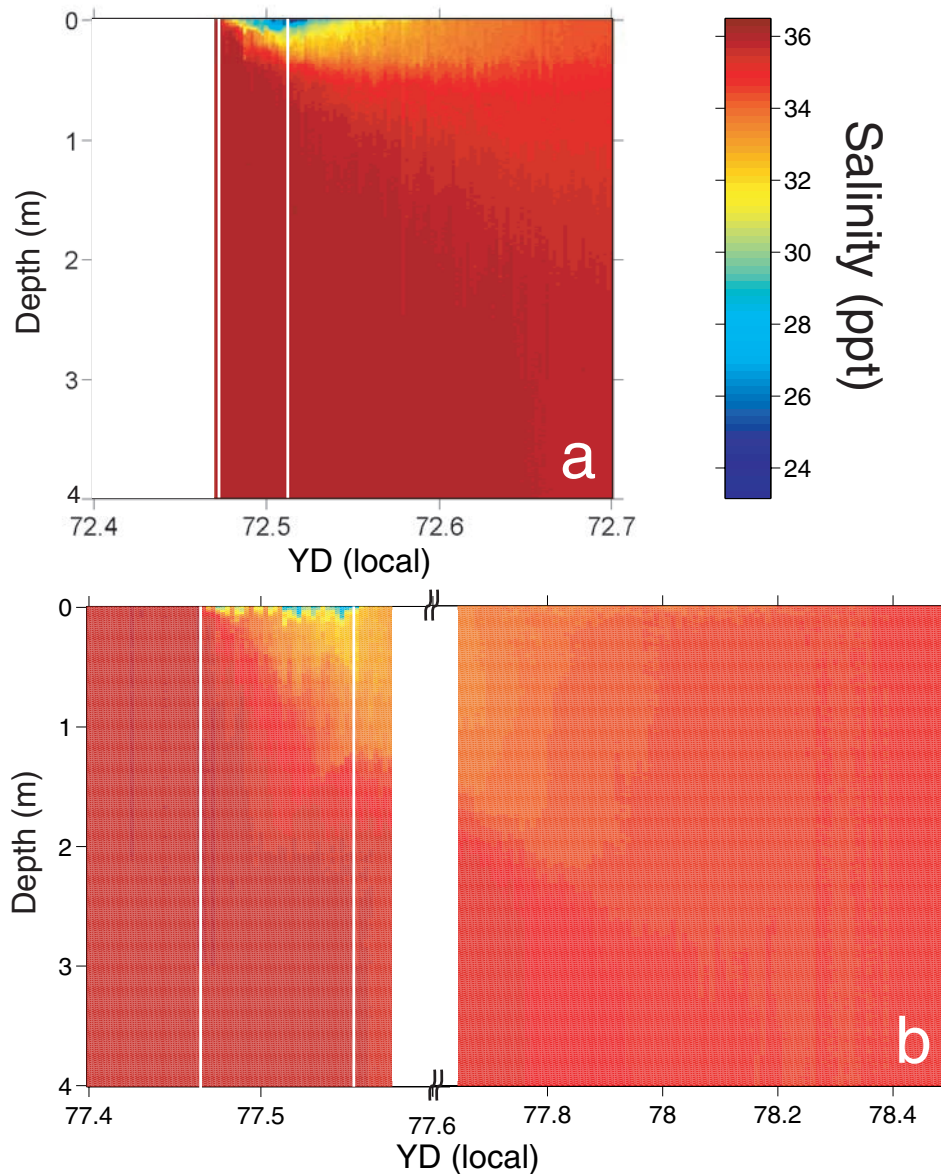
Figure 6. Time series plot of density from SkinDeEP for (a) RE1 and (b) RE2 over the upper 4 m of the Biosphere 2 ocean. The white vertical lines bracket the period of rainfall. Note the change in the timescale in Figure 6b after YD 77.6. The gap in the data occurred when SkinDeEP was recovered for reprogramming of the instrument to change the profile interval.

scale is comparable to small breaking waves. As the cumulative number of drops increases with time, more of the surface is disrupted by rain. This process significantly enhances mixing. Figure 9d shows that the turbulent disruptions of the TBL by raindrops have reached a level of steady state saturation. Comparing Figures 9a and 9d, it is clear that the surface mixing due to rain is complete in its spatial extent. The turbulence due to the raindrops now dominates over the buoyancy-driven circulation that dominated previous to the inception of rain. The raindrops are ubiquitous, and the uniform surface mixing and subsequent air-water gas exchange are comparable to other seemingly more energetic processes such as wave breaking.

[53] Using λ calculated from IR imagery, $k(600)$ was determined using equation (11) to be 8.7 ± 0.7 cm h^{-1} for

no rain conditions, and increased to 23.7 ± 2.3 cm h^{-1} during the rain event.

4. Discussion

[54] The results presented here clearly show that rainfall on the ocean enhances the rate of air-sea gas exchange. $k(600)$ was 49.7 ± 5.4 cm h^{-1}, with energy input from the wave generator, the circulation pumps, and from rain. The $k(600)$ for no rain conditions was 11.2 ± 0.3 cm h^{-1}, so the difference in $k(600)$ between the rain and no rain conditions is 38.5 cm h^{-1}. This value is slightly higher than predicted by the relationship between KEF and $k(600)$ established by *Ho et al.* [1997], 33.2 cm h^{-1} for a KEF of 0.37 J m^{-2} s^{-1}, but the combined effect of rain and waves is unlikely to be additive.
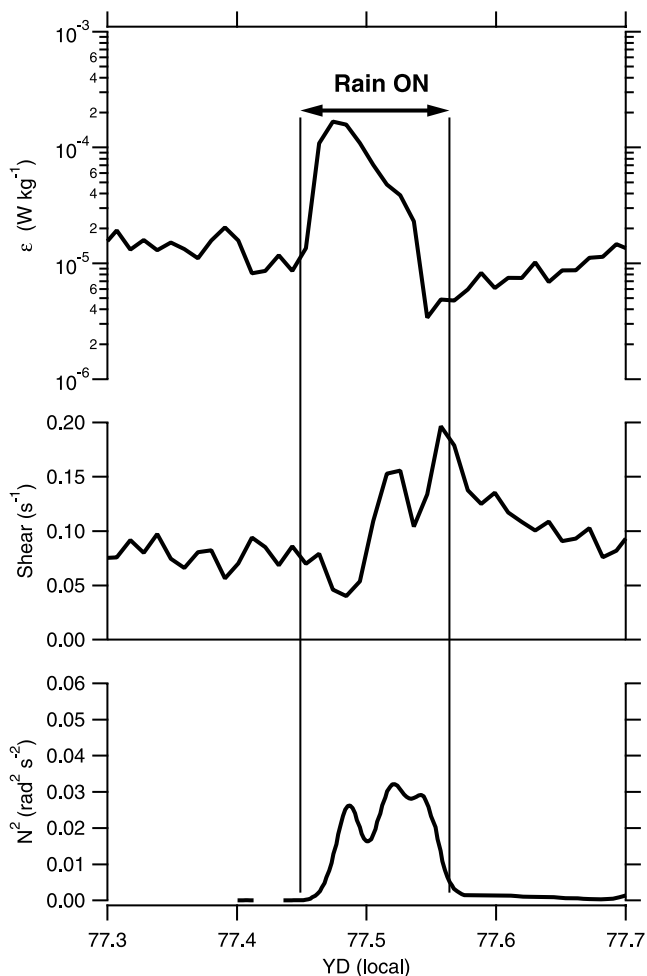
Figure 7. Plots of turbulent kinetic energy dissipation rate (ε) at a depth of 20 cm, shear across a depth of 5 to 20 cm, and Brunt-Väisälä frequency squared (N^2) across a depth of 5 to 20 cm, before, during, and after RE2.

It is possible that the situation is analogous to rain- and wind-generated turbulence. Rain penetrates the water surface and generates turbulence. At the same time, rain has also been shown to alter wind-generated waves [*Poon et al.*, 1992; *Tsimplis and Thorpe*, 1989; *Tsimplis*, 1992], which in turn affects wind-wave generated turbulence [*Jones*, 1985; *Terray et al.*, 1996]. At this point, it is not clear how much of the measured $k(600)$ can be attributed to the rain, and how much is due to the waves and currents. For no rain conditions, $k(600)$ in the Biosphere 2 ocean is comparable to that predicted for the open-ocean at a wind speed of 5.2 m s^{-1} [*Wanninkhof*, 1992], suggesting that the system is artificially energetic. More systematic experiments and a better understanding of the underlying mechanism might allow these two effects to be separated.

[55] Even though rain-induced $k(600)$ was similar for both fresh and saltwater, the overall rain-induced gas fluxes were quite different, due to the difference in C_w. Calculations using equation (3) indicate that rain-induced gas flux in saltwater, assuming that influence of rain, circulation pumps, and wave generator were additive, was ~30% of the flux measured in freshwater. Since the major difference between previous experiments conducted in freshwater and

Bio2 RainX II is the density stratification caused by freshwater falling on saltwater for the present experiment, the decrease in gas flux is most likely due to decrease in vertical mixing caused by the density stratification (i.e., decrease in how quickly mass was moved up to the air-water interface to be exchanged).

[56] The SF$_6$ evasion result showing an increase in $k(600)$ due to rain is consistent with physical measurements made during RE2. Turbulence generated during the rain events due to the impact of raindrops on the water surface is expected to control gas transfer. Rainfall delivers turbulent kinetic energy to the surface layer of the ocean, causing an increase in ε (Figure 8). Following this increase in ε, stable stratification builds up (increase in N^2) due to the addition of freshwater by rain and suppresses turbulent mixing near the surface, causing ε to decrease substantially. The input of turbulent kinetic energy by the rain is now transferred to the buildup of shear in the near surface until the rain ends. However, following the turbulent kinetic energy budget for steady state homogeneous conditions, the decrease in ε during this time suggests that the mechanical production of turbulence due to shear is not able to overcome the density stratification. Following the completion of the rainfall, density stratification rapidly breaks down due to the vigorous background ocean mixing, and ε and shear come to equilibrium at levels that are comparable to those in the pre-rain background.

[57] During Bio2 RainX II, near-surface ε ranged from 10^{-6} W kg^{-1} in the absence of rain to 10^{-4} W kg^{-1} during RE2 as shown in Figure 8, and observed for RE1 and RE3. For comparison, estimates of ε beneath breaking waves on Lake Ontario ranged from 10^{-5} to 10^{-2} W kg^{-1} [*Agrawal et al.*, 1992; *Terray et al.*, 1996] and energetic mixed layers show ε values from 10^{-6} to 10^{-4} W kg^{-1} [*MacIntyre et al.*, 1995]. In comparison to these open-ocean systems, estimates of near-surface ε under low wind conditions in
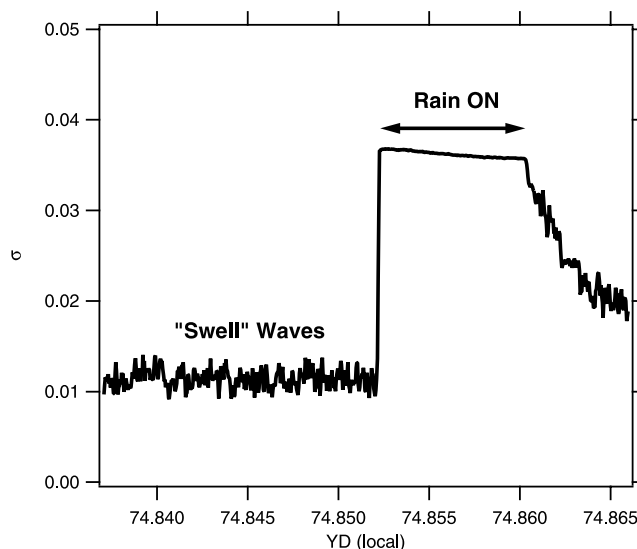
Figure 8. Plot of inverted squared laser light intensity (σ) measured during RE3 by the laser slope zero-crossing meter before, during, and after the rain event. Higher values denote a water surface that is abundant with small-scale, steeply sloped waves.
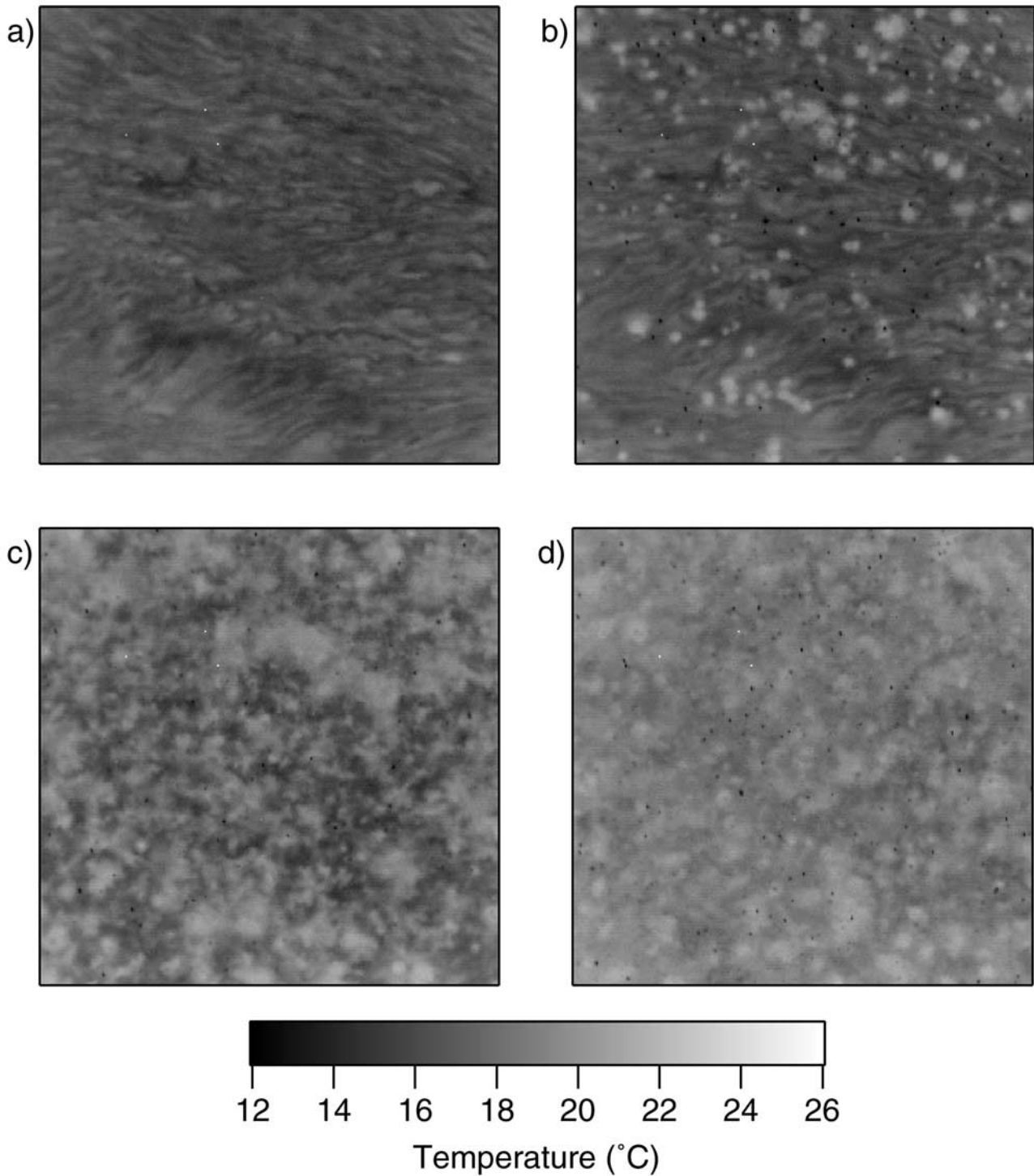
Figure 9. Snapshots of infrared imagery during the course of RE3. The image size is 2 × 2 m and the temperature variability is 1°C. (a) The Biosphere 2 ocean before the rain began. (b) The onset of rain (black dots in the image) produces localized mixing of the TBL to produce warm patches of water. (c) Rain continues to mix the aqueous surface boundary layer. (d) Fully developed rain causing the surface of the ocean to be intensely mixed.

the Parker River of northeastern Massachusetts ranged from 10^{-6} to 10^{-4} W kg^{-1} [*Zappa et al.*, 2003] and in the Hudson River near Manhattan ranged from 10^{-7} to 10^{-6} W kg^{-1} during neap tides and from 10^{-7} to 10^{-5} W kg^{-1} during spring tides [*Peters and Bokhorst*, 2000]. This comparison suggests that in the absence of rain, the Biosphere 2 ocean exhibits near-surface ε similar to estuarine systems of varying size under comparably low wind

speeds during lower flow phases of the tide, and comparable to weaker mixed layers. Our results demonstrate that rain significantly enhances turbulence under no wind conditions in the Biosphere 2 ocean, comparable to highly energetic mixed layers, but significantly less than that found beneath breaking waves.

[58] The $k(600)$ calculated from the surface renewal (SR) and the dissipation rate (DR) methods are comparable, and show increasing $k(600)$ during the rain events, suggesting that these estimates of $k(600)$ may prove to be useful in developing statistical models for rain-induced gas exchange that encompass the underlying processes and mechanisms. However, the estimates of $k(600)$ from SR and DR are lower than $k(600)$ determined by SF_6 evasion. The passive SR method may underestimate $k(600)$ derived from SF_6 because the resolution of the IR imager used during Bio2 RainX II is large relative to the smallest scale fluctuations, i.e., surface renewal. The SR method may be improved by increasing the resolution of the IR imagery to capture the smallest scales of turbulence affecting the air-water interface, and by implementing the active controlled flux technique [e.g., *Jähne and Haußecker*, 1998; *Asher et al.*, submitted; *Atmane et al.*, 2004; *Zappa et al.*, 2003, submitted manuscript, 2004]. While the DR method captures the variability of $k(600)$ comparable to the SR method, the SR method may prove to be more powerful since it directly measures surface renewal using IR imagery of the air-water interface. The DR method uses ε measured at depth (∼20 cm) and may not capture the effects of processes occurring near the air-water interface (e.g., near-surface shear, stratification, surfactants), which could lead to errors in estimating $k(600)$.

[59] Profiles of SF_6, density, and also calculated N^2 from 5 to 20 cm depth show that the stratification created by rain falling on the ocean is quickly broken after 1–2 hours (Figures 4, 6, 8). The relatively high turbulent energy in the Biosphere 2 ocean is presumably responsible for the rapid mixing. For comparison, data from the western equatorial Pacific Ocean show that the situation at Biosphere 2 is not anomalous. Following a 1-hour rain event at 20–30 mm h^{-1}, a fresh water anomaly formed on the ocean surface. However, mixing and advection causes surface salinity to rapidly increase such that within 5 hours, the low-salinity anomaly had deepened to 40 m [*Wijesekera et al.*, 1999].

[60] Measurements made during RE3 show evidence of significant increase in rain-generated small-scale, steeply sloped capillary waves (Figure 9), which have been shown to correlate with an increase in k [*Bock et al.*, 1999; *Jähne et al.*, 1987]. These steep small-scale waves have been modeled [*Szeri*, 1997] and experimentally observed [*Saylor and Handler*, 1997] to directly enhance gas transfer through surface renewal. Furthermore, the IR measurements show an increase in surface renewal due to rain-induced surface turbulence, consistent with the increase in ε and k. However, the relative importance of, or link between, rain-induced near-surface turbulence and capillary waves is difficult to discern from these measurements, and future controlled experiments may successfully address this issue. There are various mechanisms by which rain is known to dampen waves and modify surface wave conditions [e.g., *Tsimplis and Thorpe*, 1989; *Tsimplis*, 1992]. Rain-produced small-scale wavelets provide an attenuating mechanism by taking energy from the underlying wave field through nonlinear wave-wave interactions. Rain may also modify the damping of waves by modulating any existing surfactants through bubble production or mixing with the underlying fluid. Rain also changes the temperature and salinity of water, and thereby changing its kinematic viscosity. Finally, vortex rings generated by raindrops have been suggested as the mixing mechanism responsible not only for wave damping but also for the generation of near-surface turbulence. Although not all drops create vortex rings, rainfall generates subsurface turbulence, which has been shown to enhance gas transfer and to explain the damping of waves with wavelengths of less than 30 cm. All of these processes contribute to modifying near-surface turbulence and the wave characteristics during rainfall.

[61] The "swell" waves in the Biosphere 2 ocean are roughly an order of magnitude smaller in H_s when compared to the recent GasEx II field experiment in the eastern equatorial Pacific (W. McGillis et al., Air-sea CO_2 exchange in the equatorial Pacific, submitted to *Journal of Geophysical Research*, 2004). Analogously, the dominant wave period in the Biosphere 2 ocean is shorter than is observed in the open ocean by an order of magnitude or more. Therefore the energetics of the "swell" waves on the Biosphere 2 ocean are not comparable to those of the deep-ocean swell. Since short, steep wind-driven waves have been shown to be important in air-sea gas exchange [*Bock et al.*, 1999; *Jähne et al.*, 1987; *Zappa et al.*, 2001, submitted manuscript, 2004], the longer, low-amplitude "swell" in the Biosphere 2 ocean is not expected to control gas exchange in the absence of wind.

5. Conclusions

[62] Because only one rain rate was used during Bio2 RainX II, no general relationship between rain rate and air-sea gas exchange could be derived. However, the results of the experiment indicate that rain enhances the rate of gas exchange in the ocean, as it does in freshwater, even though the overall gas flux is mitigated by density stratification. Also, the SF_6 tracer result is consistent with physical measurements made concurrently during the experiment.

[63] Although much has been learned about the influence of rain on air-water gas exchange, some questions remain. The effect of rain on air-water gas exchange has been documented previously in laboratory experiments in freshwater [*Ho et al.*, 1997] and now in saltwater at Biosphere 2. The role of bubbles was quantified and that of rain-generated turbulence was inferred [*Ho et al.*, 2000] for freshwater. Here, for the first time during a gas exchange experiment, the turbulent kinetic energy dissipation rate under rainfall was measured, and the wave properties and IR signature were documented. However, systematic measurements of these properties remain to be made. Also, there have only been a few gas exchange experiments in the natural environment where rain-forcing has been considered [*Cole and Caraco*, 1998; *Frost and Upstill-Goddard*, 2002], and no systematic studies have been conducted. The mechanisms behind rain-induced gas exchange, and the interaction of rain- and wind-generated waves and turbulence, should be examined in greater depth.

[64] Once the mechanism behind rain-induced gas exchange has been sufficiently understood and the process is documented in nature, the ecosystem and global implications of rain-induced gas exchange can be assessed. The following questions should be answered: On an ecosystem scale, how important is rain-induced gas exchange in quiescent environments such as wetlands, where some gas flux might also be facilitated through macrophytes [e.g., *Dacey and Klug*, 1979]. Globally, how large of a role does rain-induced gas exchange play in the uptake of atmospheric CO_2 by the ocean, and exchange of other biogeochemical trace gases?

References

Agrawal, Y. C., E. A. Terray, M. A. Donelan, P. A. Hwang, A. J. Williams III, W. M. Drennan, K. K. Kahma, and S. A. Kitaigorodskii (1992), Enhanced dissipation of kinetic energy beneath surface waves, *Nature*, 359, 219–220.

Asher, W. E., and J. F. Pankow (1986), The interaction of mechanically generated turbulence and interfacial films with a liquid phase controlled gas/liquid transport process, *Tellus*, 38, 305–318.

Asher, W. E., A. T. Jessup, and M. Atmane (2004), Oceanic application of the active controlled flux technique for measuring air-sea transfer velocities of heat and gases, *J. Geophys. Res.*, 109, C08S12, doi:10.1029/2003JC001862, in press.

Atkinson, M. J., H. Barnett, H. Aceves, C. Langdon, S. J. Carpenter, T. McConnaughey, E. Hochberg, M. Smith, and B. D. V. Marino (1999), The Biosphere 2 coral reef biome, *Ecol. Eng.*, 13, 147–171.

Atmane, M., W. E. Asher, and A. T. Jessup (2004), On the use of the active infrared technique to infer heat and gas transfer velocities at the air-water free surface, *J. Geophys. Res.*, C08S14, doi:10.1029/2003JC001805, in press.

Bock, E. J., T. Hara, N. M. Frew, and W. R. McGillis (1999), Relationship between air-sea gas transfer and short wind waves, *J. Geophys. Res.*, 104, 25,821–25,831.

Brumley, B. H., and G. H. Jirka (1988), Air-water transfer of slightly soluble gases: Turbulence, interfacial processes and conceptual models, *Physicochem. Hydrodyn.*, 10, 295–319.

Cole, J. J., and N. F. Caraco (1998), Atmospheric exchange of carbon dioxide in a low-wind oligotrophic lake measured by the addition of SF_6, *Limnol. Oceanogr.*, 43, 647–656.

Craeye, C., and P. Schlussel (1998), Rainfall on the sea: Surface renewals and wave damping, *Boundary Layer Meteorol.*, 89, 349–355.

Dacey, J. W. H., and M. J. Klug (1979), Methane efflux from lake-sediments through water lilies, *Science*, 203, 1253–1255.

Danckwerts, P. V. (1951), Significance of liquid-film coefficients in gas absorption, *Ind. Eng. Chem. Res.*, 43, 1460–1467.

Donlon, C. J., and I. S. Robinson (1997), Observations of the oceanic thermal skin in the Atlantic Ocean, *J. Geophys. Res.*, 102, 18,585–18,606.

Frew, N. M. (1997), The role of organic films in air-sea gas exchange, in *The Sea Surface and Global Change*, edited by P. S. Liss and R. A. Duce, pp. 121–172, Cambridge Univ. Press, New York.

Frost, T., and R. C. Upstill-Goddard (2002), Meteorological controls of gas exchange at a small English lake, *Limnol. Oceanogr.*, 47, 1165–1174.

Hill, R. H. (1972), Laboratory measurement of heat transfer and thermal structure near an air-water interface, *J. Phys. Oceanogr.*, 2, 190–198.

Ho, D. T., L. F. Bliven, R. Wanninkhof, and P. Schlosser (1997), The effect of rain on air-water gas exchange, *Tellus, Ser. B*, 49, 149–158.

Ho, D. T., W. E. Asher, L. F. Bliven, P. Schlosser, and E. L. Gordan (2000), On mechanisms of rain-induced air-water gas exchange, *J. Geophys. Res.*, 105, 24,045–24,057.

Jähne, B., and H. Haußecker (1998), Air-water gas exchange, *Ann. Rev. Fluid Mech.*, 30, 443–468.

Jähne, B., K. O. Münnich, and U. Siegenthaler (1979), Measurements of gas exchange and momentum transfer in a circular wind tunnel, *Tellus*, 31, 321–329.

Jähne, B., W. Huber, A. Dutzi, T. Wais, and J. Ilmberger (1984), Wind/wave-tunnel experiment on the Schmidt number—And wave field dependence of air/water gas exchange, in *Gas Transfer at Water Surfaces*, edited by W. Brutsaert and G. H. Jirka, pp. 303–309, D. Reidel, Norwell, Mass.

Jähne, B., T. Wais, L. Memery, G. Caulliez, L. Merlivat, K. O. Münnich, and M. Coantic (1985), He and Rn gas exchange experiments in the large wind-wave facility of IMST, *J. Geophys. Res.*, 90, 11,989–11,997.

Jähne, B., K. O. Munnich, R. Bosinger, A. Dutzi, W. Huber, and P. Libner (1987), On the parameters influencing air-water gas exchange, *J. Geophys. Res.*, 92, 1937–1949.

Jessup, A. T., C. J. Zappa, and H. Yeh (1997), Defining and quantifying microscale wave breaking with infrared imagery, *J. Geophys. Res.*, 102, 23,145–23,154.

Jones, I. S. F. (1985), Turbulence below wind waves, in *The Ocean Surface—Wave Breaking, Turbulent Mixing and Radio Probing*, edited by Y. Toba and H. Mitsuyasu, pp. 437–442, D. Reidel, Norwell, Mass.

Katsaros, K. B. (1977), The sea surface temperature deviation at very low wind speeds; Is there a limit?, *Tellus*, 29, 229–239.

Katsaros, K. B. (1980), The aqueous thermal boundary layer, *Boundary Layer Meteorol.*, 18, 107–127.

Katsaros, K. B., W. T. Liu, J. A. Businger, and J. E. Tillman (1977), Heat transport and thermal structure in the interfacial boundary layer measured in an open tank of water in turbulent free convection, *J. Fluid Mech.*, 83, 311–335.

Lamont, J. C., and D. S. Scott (1970), An eddy cell model of mass transfer into the surface of a turbulent liquid, *AIChE J.*, 16, 513–519.

Ledwell, J. R. (1982), Gas exchange across the air-water interface, Ph.D. dissertation, Harvard Univ., Cambridge Mass.

Ledwell, J. R. (1984), The variation of the gas transfer coefficient with molecular diffusivity, in *Gas Transfer at Water Surfaces*, edited by W. Brutsaert and G. H. Jirka, pp. 293–302, D. Reidel, Norwell, Mass.

Lhermitte, R. (1988), Cloud and precipitation sensing at 94 GHz, *IEEE Trans. Geosci. Remote Sens.*, 26, 207–216.

Liss, P. S., and L. Merlivat (1986), Air-sea gas exchange rates: Introduction and synthesis, in *The Role of Air-Sea Exchange in Geochemical Cycling*, edited by P. Buat-Ménard, pp. 113–127, D. Reidel, Norwell, Mass.

MacIntyre, S., R. Wanninkhof, and J. P. Chanton (1995), Trace gas exchange across the air-water interface in freshwater and coastal marine environments, in *Biogenic Trace Gases: Measuring Emissions From Soil and Water*, edited by R. C. Harriss and P. A. Matson, pp. 52–97, Blackwell Sci., Cambridge, Mass.

Marshall, J. S., and W. M. Palmer (1948), The distribution of the raindrops with size, *J. Meteorol.*, 5, 165–166.

McAlister, E. D. (1964), Infrared-optical techniques applied to oceanography: I. Measurement of total heat flow from the sea surface, *Appl. Optics*, 3, 609–612.

McAlister, E. D., and W. McLeish (1969), Heat transfer in the top millimeter of the ocean, *J. Geophys. Res.*, 74, 3408–3414.

McAlister, E. D., and W. McLeish (1970), A radiometric system for airborne measurement of the total heat flow from the sea, *Appl. Opt.*, 9, 2697–2705.

Nightingale, P. D., G. Malin, C. S. Law, A. J. Watson, P. S. Liss, M. I. Liddicoat, J. Boutin, and R. C. Upstill-Goddard (2000), In situ evaluation of air-sea gas exchange parameterizations using novel conservative and volatile tracers, *Global Biogeochem. Cycles*, 14, 373–387.

Olsen, R. L., D. V. Rogers, and D. B. Hodge (1978), Arb relation in calculation of rain attenuation, *IEEE Trans. Antennas Propag.*, 26, 318–329.

Peters, H., and R. Bokhorst (2000), Microstructure observations of turbulent mixing in a partially mixed estuary: I. Dissipation rate, *J. Phys. Oceanogr.*, 30, 1232–1244.

Poon, Y.-K., S. Tang, and J. Wu (1992), Interactions between rain and wind waves, *J. Phys. Oceanogr.*, 22, 976–987.

Robinson, I. S., N. C. Wells, and H. Charnock (1984), The sea surface thermal boundary layer and its relevance to the measurement of sea surface temperature by airborne and spaceborne radiometers, *Int. J. Remote Sens.*, 5, 19–45.

Saunders, P. M. (1967), The temperature at the ocean-air interface, *J. Atmos. Sci.*, 24, 269–273.

Saylor, J. R., and R. A. Handler (1997), Gas transport across an air/water interface populated with capillary waves, *Phys. Fluids*, 9, 2529–2541.

Saylor, J. R., B. K. Jones, and L. F. Bliven (2002), A method for increasing depth of field during droplet imaging, *Rev. Sci. Instrum.*, 73, 2422–2427.

Schlüssel, P., W. J. Emery, H. Grassl, and T. Mammen (1990), On the bulk-skin temperature difference and its impact on satellite remote sensing of sea surface temperature, *J. Geophys. Res.*, 95, 13,341–13,356.

Szeri, A. J. (1997), Capillary waves and air-sea gas transfer, *J. Fluid Mech.*, *332*, 341–358.

Terray, E. A., M. A. Donelan, Y. C. Agrawal, W. M. Drennan, K. K. Kahma, I. A. J. Williams, P. A. Hwang, and S. A. Kitaigorodskii (1996), Estimates of kinetic energy dissipation under surface waves, *J. Phys. Oceanogr.*, *26*, 792–807.

Tsimplis, M. N. (1992), The effect of rain in calming the sea, *J. Phys. Oceanogr.*, *22*, 404–412.

Tsimplis, M., and S. A. Thorpe (1989), Wave damping by rain, *Nature*, *342*, 893–895.

Wanninkhof, R. (1992), Relationship between gas exchange and wind speed over the ocean, *J. Geophys. Res.*, *97*, 7373–7381.

Wanninkhof, R., and W. R. McGillis (1999), A cubic relationship between air-sea CO_2 exchange and wind speed, *Geophys. Res. Lett.*, *26*, 1889.

Wanninkhof, R., J. R. Ledwell, W. S. Broecker, and M. Hamilton (1987), Gas exchange on Mono Lake and Crowley Lake, California, *J. Geophys. Res.*, *92*, 14,567–14,580.

Ward, B., R. Wanninkhof, P. J. Minnett, and M. Head (2004), SkinDeEP: A profiling instrument for upper decameter sea surface measurements, *J. Atmos. Oceanic Technol.*, *21*, 207–222.

Wick, G. A., W. J. Emery, L. H. Kantha, and P. Schlüssel (1996), The behavior of the bulk-skin sea surface temperature difference under varying wind speed and heat flux, *J. Phys. Oceanogr.*, *26*, 1969–1988.

Wijesekera, H. W., C. A. Paulson, and A. Huyer (1999), The effect of rainfall on the surface layer during a westerly wind burst in the western equatorial Pacific, *J. Phys. Oceanogr.*, *29*, 612–632.

Wu, J. (1971), An estimation of oceanic thermal-sublayer thickness, *J. Phys. Oceanogr.*, *1*, 284–286.

Zappa, C. J. (1999), Microscale wave breaking and its effect on air-water gas transfer using infrared imagery, Ph.D. thesis, Univ. of Wash., Seattle.

Zappa, C. J., A. T. Jessup, and H. H. Yeh (1998), Skin-layer recovery of free-surface wakes: Relationship to surface renewal and dependence on heat flux and background turbulence, *J. Geophys. Res.*, *103*, 21,711–21,722.

Zappa, C. J., W. E. Asher, and A. T. Jessup (2001), Microscale wave breaking and air–water gas transfer, *J. Geophys. Res.*, *106*, 9385–9391.

Zappa, C. J., P. A. Raymond, E. A. Terray, and W. R. McGillis (2003), Variation in surface turbulence and the gas transfer velocity over a tidal cycle in a macro-tidal estuary, *Estuaries*, *26*, 1401–1415.

———————————

L. F. Bliven, NASA/GSFC, Laboratory for Hydrospheric Processes, Wallops Island, VA 23337, USA. (francis.l.bliven@nasa.gov)

J. W. H. Dacey, Biology Department, Woods Hole Oceanographic Institution, Woods Hole, MA 02543, USA. (jdacey@whoi.edu)

M. B. Hendricks, Department of Geosciences, Princeton University, Princeton, NJ 08544, USA.

D. T. Ho, W. R. McGillis, P. Schlosser, and C. J. Zappa, Lamont-Doherty Earth Observatory, Columbia University, Palisades, NY 10964, USA. (david@ldeo.columbia.edu; mcgillis@ldeo.columbia.edu; schlosser@ldeo.columbia.edu; zappa@ldeo.columbia.edu)

B. Ward, Applied Ocean Physics and Engineering Department, Woods Hole Oceanographic Institution, Woods Hole, MA 02543, USA. (bward@whoi.edu)